Measurements of Momentum and Heat Transfer across the Air–Sea Interface

GREGORY P. GERBI AND JOHN H. TROWBRIDGE

Woods Hole Oceanographic Institution, Woods Hole, Massachusetts

JAMES B. EDSON

University of Connecticut, Storrs, Connecticut

ALBERT J. PLUEDDEMANN, EUGENE A. TERRAY, AND JANET J. FREDERICKS

Woods Hole Oceanographic Institution, Woods Hole, Massachusetts

(Manuscript received 11 December 2006, in final form 11 June 2007)

ABSTRACT

This study makes direct measurements of turbulent fluxes in the mixed layer in order to close heat and momentum budgets across the air–sea interface and to assess the ability of rigid-boundary turbulence models to predict mean vertical gradients beneath the ocean's wavy surface. Observations were made at 20 Hz at nominal depths of 2.2 and 1.7 m in ~16 m of water. A new method is developed to estimate the fluxes and the length scales of dominant flux-carrying eddies from cospectra at frequencies below the wave band. The results are compared to independent estimates of those quantities, with good agreement between the two sets of estimates. The observed temperature gradients were smaller than predicted by standard rigid-boundary closure models, consistent with the suggestion that wave breaking and Langmuir circulation increase turbulent diffusivity in the upper ocean. Similarly, the Monin–Obukhov stability function ϕ_h was smaller in the authors' measurements than the stability functions used in rigid-boundary applications of the Monin–Obukhov similarity theory. The dominant horizontal length scales of flux-carrying turbulent eddies were found to be consistent with observations in the bottom boundary layer of the atmosphere and from laboratory experiments in three ways: 1) in statically unstable conditions, the eddy sizes scaled linearly with distance to the boundary; 2) in statically stable conditions, length scales decreased with increasing downward buoyancy flux; and 3) downwind length scales were larger than crosswind length scales.

1. Introduction

The turbulence dynamics of the upper ocean dramatically affect the way that horizontal momentum and heat are transported from the surface to depth. Indeed, the century-old results of Ekman (1905) are quite sensitive to the choice and spatial structure of the turbulent diffusivity of momentum (e.g., Madsen 1977; Lentz 1995). Any attempt to parameterize accurately the effects of turbulent mixing on momentum and heat flux must account for the physical mechanisms responsible for generating turbulence.

In the ocean's surface boundary layer (mixed layer), the physical mechanisms thought to be important in turbulence production include boundary stress, boundary buoyancy flux, wave breaking, and Langmuir circulation. This study was undertaken in conditions conducive to the formation of turbulence by all of these mechanisms, and we hope that it will aid in our understanding of mixed layer turbulence dynamics and in our ability to parameterize such turbulence in closure models. Boundary stress and boundary buoyancy flux form the basis for most closure models in use today, which assume that the mixed layer behaves like a fluid flow past a rigid plate. These common models include Mellor–Yamada (Mellor and Yamada 1982), k–ε (Hanjalic and Launder 1972; Jones and Launder 1972), k–ω (Wilcox 1988), and Monin–Obukhov (MO) (Monin and Yaglom 1971), which is adapted for the ocean as the K-profile parameterization (Large et al. 1994). In recent years, several studies have adapted these closure mod-

Corresponding author address: Gregory P. Gerbi, MS 21, Woods Hole Oceanographic Institution, 360 Woods Hole Road, Woods Hole, MA 02543.
E-mail: ggerbi@whoi.edu

DOI: 10.1175/2007JPO3739.1

els to account for the effects of wave breaking and Langmuir circulation. However, the dynamics of these processes are not fully understood, and improving parameterizations of these processes will require increased understanding of how they affect mixed layer turbulence.

The effects of surface wave breaking on mixed layer turbulence have been examined observationally by several authors beginning with Agrawal et al. (1992) and Terray et al. (1996), and in models by Craig and Banner (1994) and Terray et al. (1999). Those authors suggested that wave breaking could be incorporated into the Mellor–Yamada model by introducing a source of turbulent kinetic energy at the ocean surface and by changing slightly the model's length scale equation. Breaking waves may also generate much larger-scale coherent structures, as observed in the laboratory by Melville et al. (2002). Those authors found that after a wave had broken, it left behind a coherent vortex reaching depths greater than 20% of the wavelength. This effect has yet to be observed in the field or considered in numeric models.

The effects of Langmuir circulation on mixed layer structure have also been studied observationally (Plueddemann and Weller 1999) in large-eddy simulations (LES) (e.g., McWilliams et al. 1997; Li et al. 2005), and through laboratory experiments (Veron and Melville 2001). These studies have suggested that Langmuir circulation enhances effective diffusivity and decreases vertical gradients of temperature and velocity in the boundary layer. LES models have also suggested that Langmuir circulation is quite common in the ocean (Li et al. 2005), so that its effects must be considered in mixed layer models. An attempt has been made by Kantha and Clayson (2004) to include Langmuir circulation in turbulence closure models by adding a Stokes drift production term to the turbulent kinetic energy (TKE) equation.

Direct measurements of turbulent fluxes in the ocean have only recently become reliable. In an experiment similar to the one described here, momentum flux in the surface boundary layer was measured by Cavaleri and Zecchetto (1987) as being 100 times larger than the wind stress. This mismatch was explained by Santala (1991) to be at least partly due to surface waves reflecting off the observation platform, leading to significant covariances of wave velocities. More recently, small uncertainties in sensor orientation have been identified as producing significant contamination of turbulent flux measurements by surface gravity waves (Trowbridge 1998; Shaw and Trowbridge 2001). Trowbridge (1998) and Shaw and Trowbridge (2001) also described and implemented two methods of separating turbulence information from wave contamination that rely on the assumptions that turbulent and wave velocities are uncorrelated and that the waves are coherent between sensors. With these methods, Shaw et al. (2001) and Trowbridge and Elgar (2003) made measurements of turbulent fluxes and other properties of turbulence close to the sea bed.

The present study has two principal objectives: 1) to close momentum and heat balances spanning the air–sea interface in the presence of surface waves using cospectral estimates of the turbulent fluxes, and 2) to determine the extent to which classical views of rigid-boundary turbulence describe turbulence structures, turbulent fluxes, and mean gradients in the ocean surface boundary layer. This is accomplished by means of simultaneous measurements on both sides of the air–sea interface and interpretation of the results in light of predictions based on theories from studies of the bottom boundary layer of the atmosphere. The following section describes the measurement and analysis procedures. In section 3 we present the results of our observations. These results are discussed in section 4, and finally, section 5 offers succinct conclusions of this study.

2. Methods and analysis

a. Data collection

The observations reported here were made using instruments deployed in the ocean and atmosphere at the Martha's Vineyard Coastal Observatory's (MVCO's) Air–Sea Interaction Tower, during the Coupled Boundary Layers and Air–Sea Transfer Low Winds experiment (CBLAST-Low) between 2 and 25 October 2003 [see Edson et al. (2007) for more details about the atmospheric measurements]. The tower is located about 3 km to the south of Martha's Vineyard in approximately 16 m of water (Fig. 1). The shoreline and bathymetric contours near the tower are oriented roughly east–west. Currents are dominated by semidiurnal tides, which are dominantly shore-parallel, and the mean wind direction is from the southwest.

Both oceanic and atmospheric instruments were deployed to be exposed to the dominant atmospheric forcing direction, on the southwest side of the tower. Atmospheric measurements were made at several heights between 5 and 22 m above the sea surface and include velocity, temperature, humidity, and upwelling and downwelling short- and longwave radiation (Fig. 2). Both bulk formula (Fairall et al. 2003) and direct covariance estimates of turbulent heat and momentum

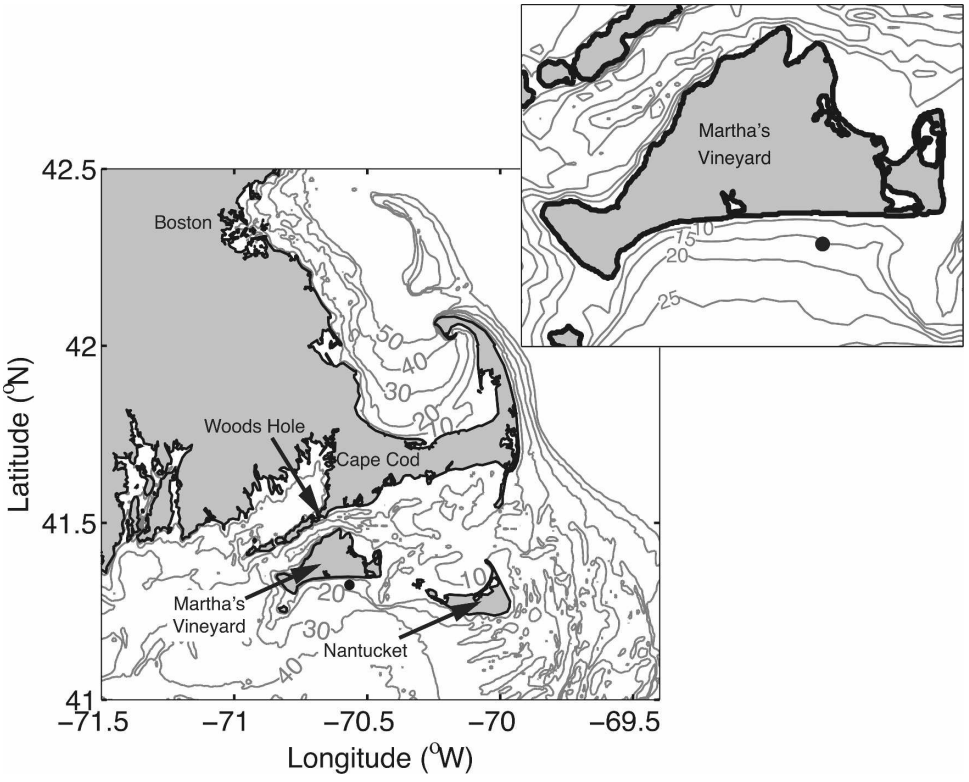

FIG. 1. Maps showing measurement location of data used in this study (dot south of Martha's Vineyard). Contours show isobaths between 10 and 50 m. The inset map shows the area in the immediate vicinity of the study site.

fluxes were made in the atmosphere, and they agree well over most wind speeds (Edson et al. 2007). The bulk formula estimates were used here to avoid data gaps in the direct covariance measurements.

In the water, measurements of turbulent velocities in the ocean were made with six Sontek 5-MHz Ocean Probe acoustic Doppler velocimeters (ADVs) mounted on a beam fixed to the tower legs (Fig. 2). The sample volumes of the ADVs were at three different depths: 2.2, 1.7, and 3.2 m below the mean surface. The deepest ADV also contained a fast-response pressure sensor. The ADVs sampled at a rate of 20 Hz in ~19-min bursts, with gaps of ~1 min between bursts. All sensors were operational for the full measurement period except for occasional times when one or more ADVs malfunctioned; these times were easily identified because they corresponded to velocity measurements of precisely zero. To minimize the effects of flow distortion through the tower, only those flows toward compass directions less than 120° clockwise from north were analyzed (Fig. 2). To avoid velocities larger than permitted by the ADV sensitivity, analysis has been limited to times when the standard deviation of vertical velocity was less than 0.16 m s^{-1}, corresponding to significant wave heights (H_s) less than ~1.4 m.

Fast response thermistors (Thermo-metrics BR14KA302G) were located near each ADV, but only two thermistors returned reliable data (ADV locations marked with u, v, w, T in Fig. 2). The thermistors were located approximately 15 cm below the sample volumes of the ADVs. Following Kristensen et al. (1997), this separation is expected to cause measured heat fluxes to deviate from actual heat fluxes by a few percent. The thermistors were operational between 11 and 25 October 2003 and measured turbulent temperature fluctuations. An upward-looking radiometer measured downwelling shortwave radiation at 4-m depth, but significant biofouling allowed only limited use of these data in the analysis presented here.

Salinity and temperature were measured at eight depths (1.4, 2.2, 3.2, 4.9, 6, 7.9, 9.9, and 11.9 m) using SeaBird MicroCATs sampling at 1-min intervals. Velocity profiles were measured with two upward-looking Nortek Aquadopp profilers. One was mounted on the bed and measured velocities in 0.5-m vertical bins. The second was mounted on the submerged beam at 4-m

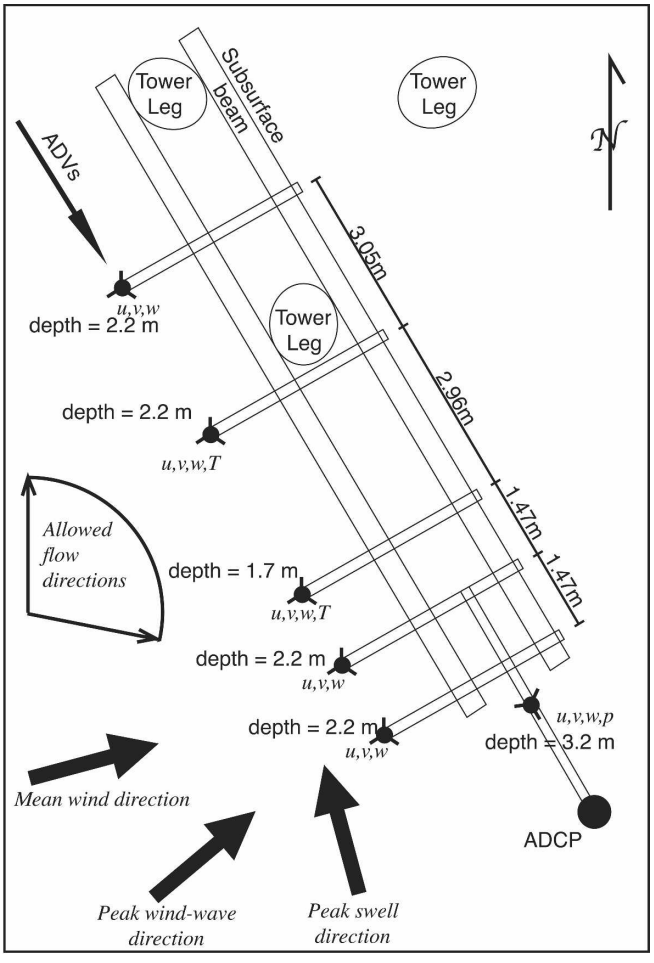

FIG. 2. Photograph, looking north, and schematic drawing of Air Sea Interaction Tower at MVCO. The platform is 12 m above the sea surface. In the schematic diagram of the instrument tower, ellipses represent the tilted tower legs (which join above the sea surface). Small filled circles with three arms each represent ADVs and thermistors. The large filled circle represents the middepth ADCP. Mean wind and wave directions are shown by boldface arrows, and the range of flow directions (0°–120°) used in this study is shown to the left.

depth and measured velocities in 0.2-m bins. Twenty-minute average pressure, for estimating tide height, was measured with a Paros pressure sensor at the MVCO seafloor node, about 1 km onshore of the measurement tower, in 12 m of water.

Because the study focused on the fluxes of momentum and heat in the boundary layer, we have analyzed flux measurements only when the ADVs were well within the mixed layer. Mixed layer depth was computed as the minimum depth at which the burst-mean temperature was more than 0.02°C less than the burst-mean temperature at the uppermost MicroCAT (following Lentz 1992). Results presented in this study are from times when the mixed layer base was at least 3.2 m below the mean sea surface.

Velocities in each burst were rotated into downwind coordinates using the mean wind direction for that burst so that x and y are coordinates in the downwind and crosswind directions, respectively, and z is the vertical coordinate, positive upward, with $z = 0$ at the burst-mean height of the sea surface, determined from pressure measurements. Instantaneous values of temperature or velocity in the (x, y, z) directions are denoted by T and (u, v, w). Conceptually, velocity and temperature observations were decomposed into mean, wave, and turbulent components, and although a specific definition is not necessary for the analysis presented here, we define wave-induced motions as those that are coherent with displacements of the free surface (e.g., Thais and Magnaudet 1996). The decomposition is

$$u = \overline{u} + \tilde{u} + u',$$

$$T = \overline{T} + \tilde{T} + T', \qquad (1)$$

with similar equations for v and w. Overbars represent a time mean over the length of the burst, $\tilde{T}$ and $(\tilde{u}, \tilde{v}, \tilde{w})$ denote wave-induced perturbations, and T' and (u', v', w') denote turbulent perturbations. By definition, means of wave and turbulent quantities are zero. In practice, the signals were decomposed in the time domain into mean parts and perturbation parts. The perturbation parts of the signal were further separated in frequency space into turbulent motions and wave motions.

The vertical Reynolds stress τ and sensible heat flux Q_s are related to turbulent velocity and temperature covariances in the following way:

$$\frac{\tau}{\rho_0} = -\overline{u'w'}, \tag{2}$$

$$\frac{Q_s}{\rho_0 C_p} = \overline{T'w'}, \tag{3}$$

where ρ_0 is a reference density and C_p is the specific heat of water.

b. Model prediction of cospectra

The principal analysis of this study involves the comparison of observed cospectra $\mathrm{Co}_{\beta w}$ (given by the real part of the cross-spectra of β and w, where β is u or T), with a two-parameter model of the turbulent cospectra based on observations from the surface boundary layer of the atmosphere. We first describe the model.

Studies in the bottom boundary layers of the atmosphere and ocean (Kaimal et al. 1972; Wyngaard and Coté 1972; Soulsby 1980; Trowbridge and Elgar 2003) have led to a semitheoretical prediction of one-dimensional turbulence cospectra as functions of wavenumber k, where $k = 2\pi/\lambda$ and λ is a turbulent length scale:

$$\frac{\mathrm{Co}_{\beta w}(k)}{\overline{\beta' w'}} = A \frac{1/k_0}{1 + \left(\dfrac{k}{k_0}\right)^{7/3}}. \tag{4}$$

For one-sided spectra,

$$A = \frac{7}{3\pi} \sin\left(\frac{3\pi}{7}\right).$$

The "rolloff wavenumber" k_0 characterizes the inverse length scale of the dominant flux-carrying eddies or, equivalently, the location of the peak of the variance-preserving cospectrum. Spectra of this form are approximately constant at small wavenumber and roll off as $k^{-7/3}$ at high wavenumber (Kaimal et al. 1972; Wyngaard and Coté 1972; Soulsby 1980). The variable parameters in the model, which are defined by the turbulence conditions, are the covariance $\overline{\beta' w'}$ and the rolloff wavenumber k_0.

Previous studies of turbulence over rigid boundaries (Wyngaard and Coté 1972; Kaimal et al. 1972; Trowbridge and Elgar 2003) have used Monin–Obukhov scaling to relate the rolloff wavenumbers to fluxes of buoyancy and momentum such that

$$k_0|z| = f(|z|/L),$$

where $|z|$ is the magnitude of the depth and the Monin–Obukhov length is defined as

$$L = \frac{\rho_0(\tau/\rho_0)^{3/2}}{\kappa g \overline{\rho' w'}}.$$

Here g is the acceleration due to gravity, ρ' is the density perturbation, and κ is von Kármán's constant, taken to be 0.4.

c. Observed cospectra

1) Wave contamination

Our array of sensors gives high-resolution frequency cospectra that contain both wave and turbulence contributions. By means of the frozen turbulence hypothesis (Taylor 1938), the model wavenumber spectrum [(4)] can be transformed into a frequency spectrum for comparison to our observations. Frequencies (inverse transit times of turbulent eddies) are related to wavenumbers (inverse length scales of turbulent eddies) by

$$\omega = kU_d, \tag{5}$$

where U_d is the steady drift speed (computed as 20-min means), and ω is radian frequency. In this study surface waves occupy the band from roughly 0.07 to 0.6 Hz, and turbulence spans frequency space below, within, and above this band.

By definition, the covariance of two signals, β and w, is the integral of the cospectrum:

$$\overline{\beta' w'} = \int_0^{\omega_{\max}} d\omega \mathrm{Co}_{\beta w}(\omega), \tag{6}$$

where $\omega_{\max}$ is the Nyquist frequency. Unlike the theoretical prediction [(4)], the observed Co_{uw} and Co_{Tw} have significant contributions in the wave band (Fig. 3b). If the cospectra are integrated over their entire frequency range, the resulting covariances are considerably scattered, and are typically one–two orders of magnitude larger than the values expected from the surface fluxes (see section 3b for discussion of the expected fluxes). This contamination has been observed in previous studies (Trowbridge and Elgar 2001; Shaw et al. 2001; Cavaleri and Zecchetto 1987) and is likely

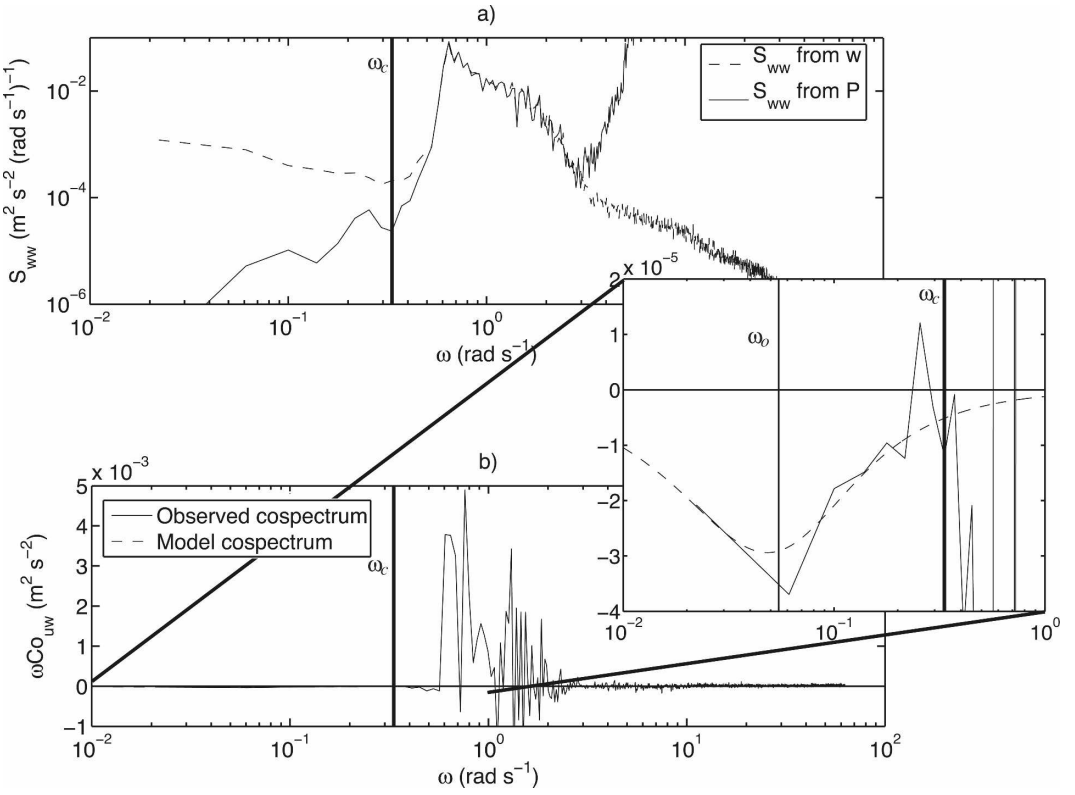

FIG. 3. (a) Autospectra of vertical velocity fluctuations for a single burst. The dashed line is the mean spectrum from the velocity records at four ADVs, and the solid line is the spectrum from a single pressure sensor and assuming a linear wave transfer function to determine the velocity spectrum [(7)]. The pressure spectrum at frequencies above 2 rad s^{-1} is dominated by white noise, causing the lack of agreement between the spectra at high frequency. The frequency band in which the two spectra overlie one another is the wave band. The thick vertical line is the wave band cutoff ω_c used for separating below–wave band (turbulence) motions from wave band motions. (b) Variance-preserving cospectra of vertical and horizontal velocity fluctuations. The solid line is an observation from a single 20-min burst on 12 Oct 2003. The dashed line is from the model [(4)] transformed by (5). The high-energy region of the data cospectrum between 0.4 and 1.5 rad s^{-1} is the part contaminated by surface waves. The low-frequency ends of the cospectra are blown up on the right to aid comparison of the model and observations. The thin vertical line is the rolloff frequency ω_0 for the model spectrum. The model-fitting procedure described in the text was only performed using information from frequencies lower than the wave band cutoff.

caused by a combination of sensor misalignment (Trowbridge 1998) and reflection of waves off the measurement platform (Santala 1991). Because wave velocities are typically much larger than those associated with turbulent motions, even a small phase shift will lead to a significant bias in the estimates of momentum and heat fluxes. In addition, the standing wave pattern due to the interference between the incident waves and those reflected from the measurement tower has a nonvanishing covariance between vertical and horizontal wave velocities, and thus contaminates the estimate of turbulent stress (note that reflected waves do not make a similar contribution to the heat flux). Following Santala (1991), we estimated the order of magnitude of this effect by computing the wave field reflected from a single vertical cylinder (Mei 1989) and found that it easily could account for the mismatch between the expected and observed momentum fluxes.

Besides contaminating the frequency cospectra, energetic surface waves can have an effect on the frozen turbulence hypothesis as addressed by Lumley and Terray (1983). Because surface waves produce oscillatory advection, even "frozen" turbulence will not have the simple relationship between wavenumber and frequency [(5)]. Instead, some low-wavenumber energy will be aliased into the wave band by the unsteady advection. Using a one-dimensional advective model, we found that unsteady advection is likely to affect our results significantly only in cases of relatively energetic waves or slow drift (see the appendix), so we have limited our observations to instances of $\sigma_U/U_d < 2$, where σ_U is the root-mean-square wave velocity. Under this

restriction, Taylor's (1938) formulation based on the mean flow speed is approximately valid, and we will use (5) to relate wavenumber and frequency spectra for frequencies lying below the wave band.

2) Separation of waves and turbulence

Because the wave spectrum overlaps the turbulence close to the rolloff frequency k_0U_d, we would, ideally, separate the waves and turbulence across all of frequency space and integrate the full turbulence cospectra to estimate the covariances of heat and momentum, as was done by Trowbridge and Elgar (2001) and Shaw et al. (2001). Unfortunately, the application of filtering schemes similar to theirs did not succeed in separating waves and turbulence in our surface layer data. Instead, we isolated the low frequency (below wave band) components of the turbulent cospectra for use in computing fluxes and flux-carrying length scales. Before describing the details of that analysis, we comment briefly on the failure of the spatial filtering approach developed by Trowbridge (1998) and Shaw and Trowbridge (2001).

Those authors were successful in applying their techniques to estimates of turbulent fluxes in the bottom boundary layer. However, in the case of surface layer observations, we found that because of the wave environment and the proximity of our instruments to the tower, the approach was unsuccessful in separating waves and turbulence. Filtering our observations reduced the scatter in the estimated covariances, relative to unfiltered data, but the variation was still an order of magnitude greater than the values expected based on the surface fluxes. This may be because the performance of the filter is degraded when more than one wave direction is present at each frequency. Multidirectional waves typically occur in surface layer measurements because of the presence of directionally spread seas, and also occur in these measurements because of the wave reflection from the tower legs. Not only does wave reflection contaminate the covariance estimates as discussed previously, it also complicates the separation of waves and turbulence by degrading the filters of Trowbridge (1998) and Shaw and Trowbridge (2001).

To separate velocities in the wave band from the below–wave band turbulent motions, we determined a wave band cutoff ω_c (see Fig. 3) for each burst. Below this cutoff, motions are presumed to be dominated by turbulence, whereas above this cutoff motions are caused by a combination of turbulence and the much more energetic surface waves. To determine the cutoff frequency we compared vertical velocity spectra derived from velocity measurements to vertical velocity spectra derived from pressure measurements using the assumption of linear surface waves (e.g., Mei 1989):

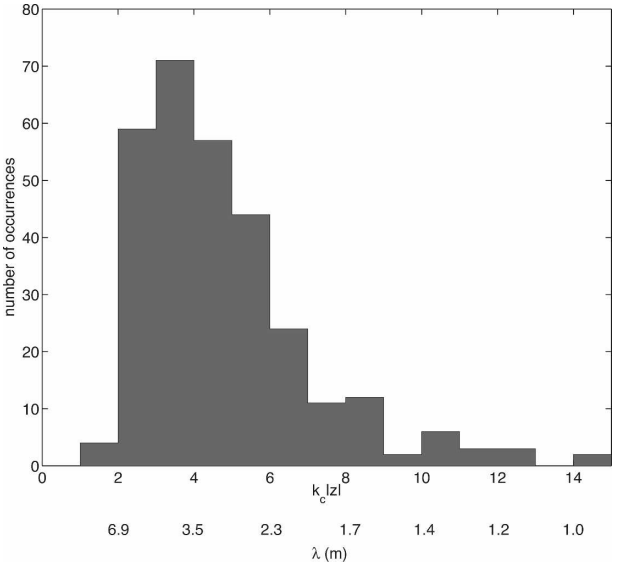

FIG. 4. Histogram of nondimensional cutoff wavenumber, $k_c|z|$, the scale of the smallest turbulent eddies measured by the below–wave band cospectral method, normalized by depth. A second x-axis scale gives the equivalent cutoff length scales, $\lambda = 2\pi/k_c$, at a nominal depth of 2.2 m.

$$S_{ww}^{(p)} = S_{pp}\frac{k^2}{\rho_0^2\omega^2}\tanh^2 k(z + h), \tag{7}$$

where $S_{ww}^{(p)}$ is the vertical velocity spectrum derived from pressure measurements, S_{pp} is the pressure spectrum, and h is the water depth. At low frequencies, most of the vertical velocity fluctuations are related to turbulent motions, so $S_{ww}^{(p)}$ is expected to be smaller than S_{ww}, the vertical velocity spectrum derived directly from velocity measurements. In the wave band, however, the vertical velocity fluctuations are dominated by wave motions, so $S_{ww}^{(p)}$ is expected to be approximately equal to S_{ww}. The wave band cutoff was chosen as the frequency at which $S_{ww}^{(p)}$ equaled 30% of S_{ww} (see Fig. 3a) such that

$$S_{ww}^{(p)}(\omega_c) = 0.3S_{ww}(\omega_c).$$

The cutoff frequency represents the transit time past the sensors of the smallest eddies resolved in the below–wave band flux estimates. By means of (5), the cutoff frequency gives a cutoff wavenumber, k_c, which, in turn, gives the minimum resolved length scale of the below–wave band turbulence. These minimum resolved length scales are generally less than twice the measurement depth (Fig. 4). Note that the cutoff wavenumber k_c is a property of the wave field, whereas the rolloff wavenumber k_0 is a property of the turbulence.

d. Cospectral estimates of turbulent fluxes and rolloff frequencies

Estimates of covariance explained by turbulent motions, $\overline{u'w'}$ and $\overline{T'w'}$, and rolloff wavenumbers, k_{0uw} and k_{0Tw}, were computed by fitting the model cospectrum (4) to the observed below–wave band cospectra. Our hypothesis in this fitting is that momentum and heat are transported in the upper ocean by turbulence with scales similar to those predicted based on studies in the bottom boundary layers of the ocean and atmosphere. If that hypothesis is correct, then the results of this fitting procedure should give reliable estimates of the turbulent properties, $\overline{u'w'}$, $\overline{T'w'}$, k_{0uw}, and k_{0Tw}, which will be tested as described in sections 3b and 3e. Although the model was developed for turbulence in the atmospheric boundary layer, we believe that it is adequate for describing the low-wavenumber cospectra that are expected from turbulent fluctuations in the mixed layer. The model cospectrum describes turbulence created at a large length scale, $\lambda_0 = 2\pi/k_0$, that cascades to smaller scales in an inertial range with a logarithmic spectral slope of −7/3. The principal difference that we might expect in the mixed layer is a different spectral slope; because the fitting is done only for low wavenumbers, the model fitting procedure is relatively insensitive to the value of that spectral slope.

Because the instrument array had four ADVs at 2.2-m depth, the four velocity cospectra at that depth were averaged together before the fitting was performed. In all other cases (Co_{uw} at 1.7 m, and Co_{Tw} at 2.2 and 1.7 m) cospectra from a single ADV or ADV–thermistor pair were used in the fitting. Sensitivity analyses showed that for $k_c < 2k_0$, the fitting procedure does not return reliable estimates of covariance or rolloff wavenumber, so fitting was limited to times when the wave band cutoff k_c was at least twice the model prediction of the rolloff wavenumber k_0. Approximately 15% of the observed spectra that met the criterion of k_c being at least twice the predicted k_0 could not be fit by the model with physically reasonable parameters. Criteria of distinguishing poor fits were results that deviated by a factor of 10 or more from values expected from full water column estimates or standard boundary layer theory. It is uncertain why these spectra were not well represented by the model, but they are excluded from further analysis.

3. Results

a. Quality of parameter estimates

We have applied two tests to ensure that the model cospectrum is an accurate representation of the observed below–wave band cospectra. First, we examine the nondimensional cospectra to ensure that they collapse to the form predicted by (4). The cospectral energies are normalized by the covariance estimates, $\overline{u'w'}$ or $\overline{T'w'}$, and the wavenumbers are normalized by the rolloff wavenumber estimates, k_{0uw} and k_{0Tw}. With these normalizations, the observed cospectra collapse very close to the model prediction (Fig. 5).

Second, we compare the velocity covariance estimates from the model fit, $\overline{u'w'}$, to covariance estimates computed by integrating the below–wave band part of the cospectrum, $\overline{u'w'_{\mathrm{int}}}$, where

$$\overline{u'w'_{\mathrm{int}}} = \int_0^{k_c} dk \mathrm{Co}_{uw}(k). \tag{8}$$

The model predicts that in the conditions studied here, at least 80% of the turbulent covariance is explained by below–wave band motions. The remaining 20% is explained by motions with wavenumbers within or above the wave band. Therefore, $\overline{u'w'}$ should be nearly the same as, but slightly larger than, $\overline{u'w'_{\mathrm{int}}}$. Comparison of these two covariance estimates (Fig. 6) indicates that the fitting procedure estimates fluxes larger than the direct integration estimates by about 20%, consistent with expectations.

Both of these tests suggest that the estimates of $\overline{u'w'}$,$\overline{T'w'}$, k_{0uw}, and k_{0Tw}, derived from the fit of (4) to the observations, are accurate measures of the below–wave band part of the cospectra.

b. Momentum and heat budgets

The method described above is a new technique for making cospectral estimates of turbulent covariances in the ocean. It is useful, therefore, to compare the fluxes derived from these covariance estimates with independent estimates of turbulent heat and momentum fluxes. This comparison is made by closing momentum and heat budgets across the air–sea interface. We show the development of the momentum budget for the Reynolds-averaged momentum equation in the downwind direction. The heat budget follows a similar development, and only the resulting budget will be shown. The starting momentum equation is

$$\frac{\partial \overline{u}}{\partial t} + \overline{\mathbf{u}} \cdot \boldsymbol{\nabla} \overline{u} - f\overline{v} = -\frac{1}{\rho_0}\frac{\partial \overline{p}}{\partial x} + \frac{1}{\rho_0}\frac{\partial \tau}{\partial z}, \tag{9}$$

where t is time, $\partial\overline{u}/\partial t$ is the evolution of the 20-min mean velocity, $\mathbf{u}$ is the three-dimensional velocity vector, f is the Coriolis frequency, and p is pressure. Horizontal stress divergence has been neglected.

Terms in the heat and momentum budgets not measured in this study were the barotropic and baroclinic

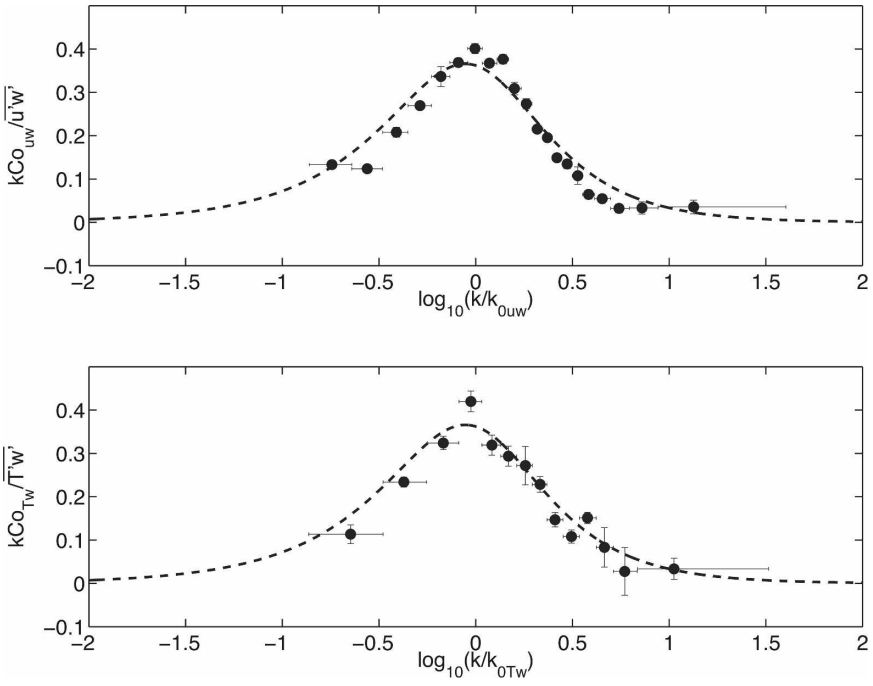

FIG. 5. Normalized variance-preserving cospectra: (top) $k\mathrm{Co}_{uw}/\mathrm{cov}_{uw}$ and (bottom) $k\mathrm{Co}_{T'w'}/\mathrm{cov}_{T'w'}$ vs normalized wavenumber k/k_0. Dots are bin averages of observations, with vertical error bars showing two standard errors of the distributions, and horizontal error bars showing the range of k/k_0 in each bin. The dashed lines show the model predictions [(4)].

pressure gradients, and the advective transports of heat and momentum. There was an array of moorings around the measurement tower, but their separations from the tower (1 to 10 km) are larger than the tidal excursion, and the array is therefore unable to measure the horizontal gradients at sufficient resolution for estimates of these terms. Instead, we rewrite the momentum budget [(9)] as deviations from its depth-averaged form:

$$\frac{\partial}{\partial t}(\overline{u} - \langle\overline{u}\rangle) + \overline{\mathbf{u}} \cdot \boldsymbol{\nabla}\overline{u} - \langle\overline{\mathbf{u}} \cdot \boldsymbol{\nabla}\overline{u}\rangle - f(\overline{v} - \langle\overline{v}\rangle) =$$

$$-\frac{1}{\rho_0}\frac{\partial}{\partial x}(\overline{p} - \langle\overline{p}\rangle) + \frac{1}{\rho_0}\frac{\partial \tau}{\partial z} - \frac{1}{\rho_0 h}(\tau_w - \tau_b), \qquad (10)$$

where

$$\langle\overline{u}\rangle = \frac{1}{h}\int_{-h}^{0} dz\, \overline{u}$$

is the vertically averaged velocity; and τ_w and τ_b are wind and bottom stress, respectively. This still leaves unmeasured the baroclinic pressure gradient and the depth-varying parts of the advective fields. In the relatively well mixed conditions studied here, those terms are expected to be small and are neglected in these budgets.

In the momentum budget we also neglect the wave growth term and the Coriolis–Stokes drift term (discussed by Hasselmann 1970; McWilliams and Restrepo

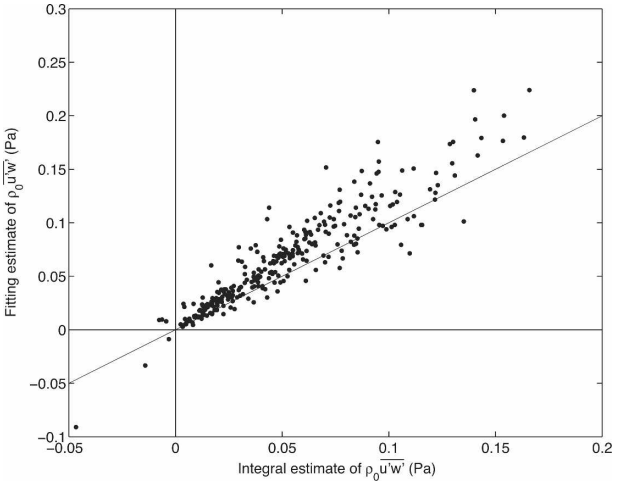

FIG. 6. Comparison of stress estimates from the two-parameter model fit (y axis) and those from the integral of below–wave band cospectra (x axis). Stresses are shown here, rather than covariance, to aid comparison with later figures.

1999; Mellor 2003; and Polton et al. 2005). Estimates of the maximum possible sizes of these terms showed them to be much smaller than the other terms in the momentum budget.

We are interested in the budget between the measurement depth and the surface, so we integrate (10) from the measurement depth z to the surface. Neglecting the depth-varying parts of the advective term and the pressure gradient we get

$$\rho_0 \int_z^0 dz \frac{\partial}{\partial t}(\overline{u} - \langle\overline{u}\rangle) - \rho_0 f \int_z^0 dz(\overline{v} - \langle\overline{v}\rangle) = \tau_w + \tau_w \frac{z}{h} - \tau_b \frac{z}{h} - \tau(z). \quad (11)$$

The last term on the right-hand side is the turbulent momentum flux and is the term that will be compared with the cospectral stress estimate. Rearranging terms, this equation becomes

$$\tau(z) = \tau_w\left(1 + \frac{z}{h}\right) - \tau_b \frac{z}{h} - \rho_0 \int_z^0 dz \frac{\partial}{\partial t}(\overline{u} - \langle\overline{u}\rangle) + \rho_0 f \int_z^0 dz(\overline{v} - \langle\overline{v}\rangle). \quad (12)$$

All of the terms on the right-hand side of (12) were evaluated from observations. The wind stress was determined from atmospheric observations, the velocity integrals were approximated using the discrete measurements of the ADCPs, and the bottom stress was estimated from the velocity of the bottom ADCP bin using a quadratic drag law:

$$\tau_b = C_d \overline{u}\sqrt{\overline{u}^2 + \overline{v}^2},$$

where $C_d = 2.0 \times 10^{-3}$ (based on unpublished direct covariance estimates of bottom stress obtained from a near-bottom array).

The heat budget is developed in an analogous way. By assuming that the heat flux through the bed is negligible and that the horizontal advective terms are vertically uniform, one obtains the sensible heat flux,

$$Q_s(z) = Q_0\left(1 + \frac{z}{h}\right) - Q_r(z) + \rho_0 C_p \int_z^0 dz \frac{\partial}{\partial t}(T - \langle T\rangle), \quad (13)$$

where Q_0 is the total surface heat flux (including sensible, latent, and radiative fluxes) and $Q_r(z)$ is the radiative heat flux in the ocean past the measurement depth. Here Q_r was computed assuming that the incoming solar radiation followed a double exponential decay profile for Jerlov type III water (Paulson and Simpson 1977; Jerlov 1968). These exponential estimates of penetrating radiation are nearly identical to the measurements of the in situ radiometer before it became significantly biofouled.

We have computed momentum and heat budgets for both measurement depths: 1.7 and 2.2 m (Fig. 7). As shown by the clustering of $\tau_w(1 + z/h)$ and $Q_0(1 + z/h)$ near the 1:1 lines, the surface flux terms are usually the largest terms in the balances. Other terms become important when surface fluxes are small and during times of downward (stabilizing) heat flux, when the penetrating radiation term (sunlight passing through the surface layer) is about half the magnitude of Q_0. All the terms except the time derivative terms are 20-min average quantities. The time derivatives were subject to significant measurement noise over time scales less than 2 h and were therefore computed as averages over 2-h periods.

c. Comparison of flux estimates

When we compare the cospectral estimates of turbulent momentum and heat fluxes with the budget estimates described above, we find that the two estimates are consistent (Fig. 8). Results are shown for sensors at 2.2- and 1.7-m depth, and for all times when mixed layers were deeper than 3.2 m. The cospectral estimates of the fluxes are scattered about the expected (budget) values. A large portion of the scatter in individual burst measurements of the fluxes is consistent with the statistical variability of the spectral estimates due to the finite length of the bursts (e.g., Soulsby 1980; Bendat and Piersol 2000).

The agreement of these two methods of measuring momentum and heat fluxes is encouraging and prompts further analysis of the turbulence dynamics.

d. Rolloff wavenumbers and turbulent length scales

In addition to fluxes, rolloff wavenumbers k_0 were also estimated by fitting the model cospectrum to the observations of the turbulent cospectra. From these rolloff wavenumbers, length scales of the dominant flux-carrying eddies, λ_0, were computed as

$$\lambda_0 = \frac{2\pi}{k_0}. \quad (14)$$

In this study, k_0 and λ_0 were estimated in the direction of the mean current, which is dominated by tidal forcing. The wind direction, however, is important for turbulence dynamics because it determines the direction of the surface stress vector. Previous measurements of turbulent length scales have been made in the directions both parallel and perpendicular to the wind or surface stress vector (Grant 1958; Wyngaard and Coté 1972; Wilczak and Tillman 1980). Grant (1958) found

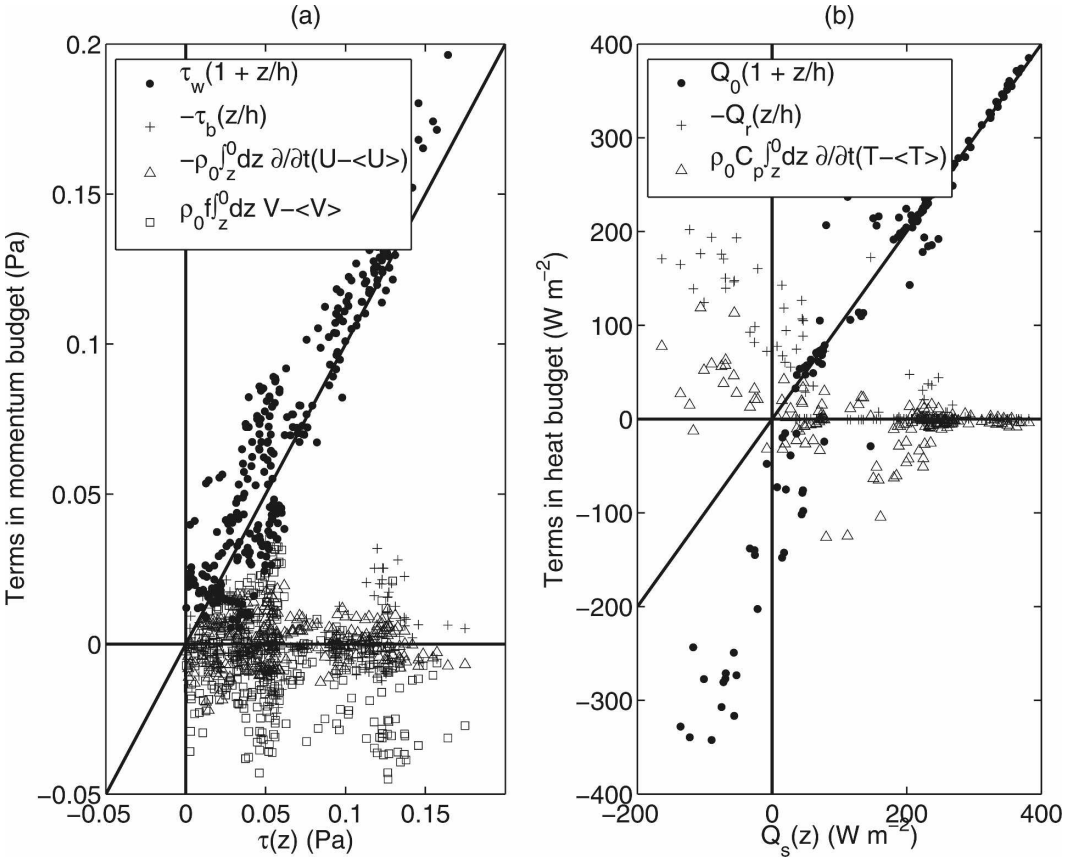

FIG. 7. Terms in the independent estimates of momentum and heat fluxes, based on budgets spanning the water between the sensor depth (nominally 2.2 and 1.7 m) and the surface. (a) The *x* axis shows the stress expected from the momentum budget and the *y* axis shows the individual terms on the right-hand side of (12). (b) The *x* axis shows the sensible heat flux expected from the heat budget, and the *y* axis shows the terms on the right-hand side of (13). The diagonal lines are 1:1. Positive heat fluxes denote heat leaving the ocean, and negative heat fluxes denote heat entering the ocean.

that under neutral conditions, turbulent eddies were coherent over much longer length scales in the stress-parallel direction than in the cross-stress direction. In marginally unstable conditions, Wilczak and Tillman (1980) also found convective plumes to be elongated in the downwind direction, although as the buoyancy forcing increased relative to the stress, they found that the crosswind scales increased relative to the downwind scales.

Wyngaard and Coté (1972) use theoretical fits to atmospheric observations to estimate the turbulent length scales λ_0 in the downwind direction, where $\lambda_0/|z| = g(|z|/L)$. In their Fig. 5, they show $g(|z|/L)$ for momentum:

$$\frac{\lambda_{0uw}}{|z|} = 8.3, \quad \frac{|z|}{L} < 0,$$
$$\frac{\lambda_{0uw}}{|z|} = 8.3\left(1 + 4.9\,\frac{|z|}{L}\right)^{-1}, \quad 0 \le \frac{|z|}{L} < 0.4 \tag{15}$$

and for heat:

$$\frac{\lambda_{0Tw}}{|z|} = 4.4, \quad \frac{|z|}{L} < 0,$$
$$\frac{\lambda_{0Tw}}{|z|} = 4.4\left(1 + 3.8\,\frac{|z|}{L}\right)^{-1}, \quad 0 \le \frac{|z|}{L} < 0.4. \tag{16}$$

These estimates of turbulent length scales from the Kansas experiment have three important properties: 1) they are constant for $|z|/L < 0$ (unstable buoyancy forcing), 2) they decrease dramatically for $|z|/L > 0$ (stable buoyancy forcing), and 3) length scales are smaller for Co_{Tw} than for Co_{uw}. Property 1 suggests that during unstable conditions, the only important length scale in setting the size of flux-carrying eddies is the distance to the boundary. Property 2 suggests that under stabilizing buoyancy flux a shorter length scale is imposed by the stratification. Finally, property 3 suggests that heat and momentum are transported by slightly different families of eddies, which may suggest that different dynam-

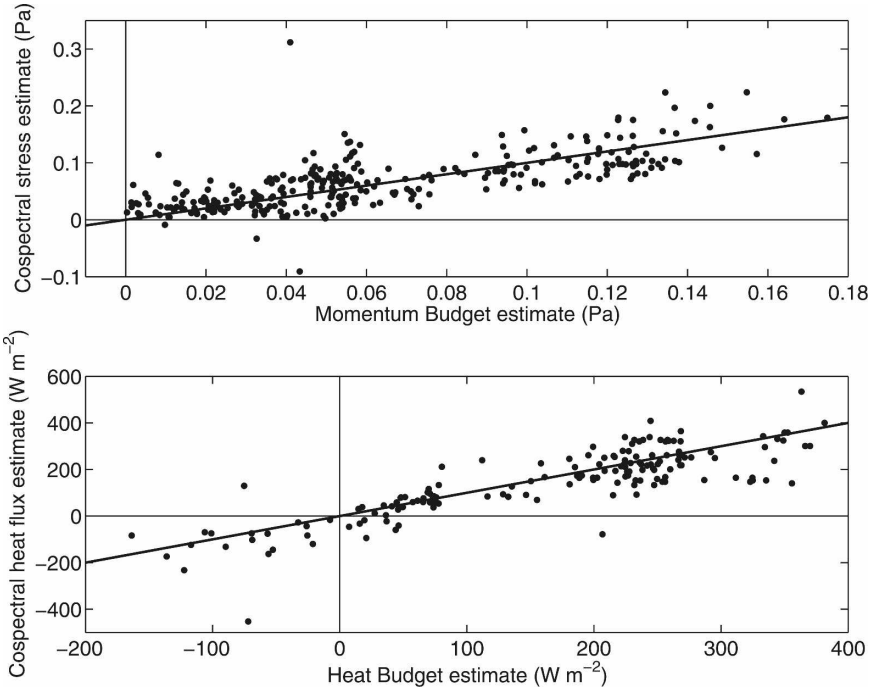

FIG. 8. Cospectral estimates of (top) momentum flux and (bottom) heat flux vs independent estimates from budgets. Dots are individual burst measurements. Data from both 1.7 and 2.2 m are shown here. A preliminary version of this figure appeared in Edson et al. (2007).

ics govern the turbulent transports of heat and momentum.

To compare our estimates of $\lambda_0|z|$ with the Wyngaard and Coté (1972) length scales, we estimated $|z|/L$ using the Monin–Obukhov scale L derived from the local estimates of momentum and heat flux. The density flux was computed from the heat flux as $\overline{\rho' w'} = \alpha \overline{T' w'}$, where α was estimated from a linear regression of 5-min averages of temperature and density over each 20-min burst. More than 85% of our observations of λ_{0uw} and more than 90% of our observations of λ_{0Tw} were made during the time of moderate buoyancy forcing, when $-1 < |z|/L < 0.4$.

We have separated observations of $\lambda_0/|z|$ for times when the mean current (drift) was approximately aligned with the wind or across the wind. Drift and wind were considered aligned when their directions were within 45° of being either parallel or antiparallel. Drift was considered crosswind when the wind and drift directions were separated by between 45° and 135°. Several features are evident in our estimates of $\lambda_0/|z|$ (Fig. 9). First, the downwind length scales are larger than the crosswind scales (cf. left panels to right panels). This is consistent with prior observations and with what is expected from Langmuir circulation. Second, for momentum, in unstable conditions ($|z|/L < 0$) the observed $\lambda_{0uw}/|z|$ are roughly constant; that is, there is little evidence for change in length scale with decreasing $|z|/L$ (Figs. 9a,b). We do not have enough observations to say conclusively that $\lambda_{0Tw}/|z|$ also is constant with $|z|/L$, but given the few observations that we have and the other similarities between λ_{0Tw} and λ_{0uw}, we expect that it is. Third, $\lambda_{0Tw}/|z|$ is generally the same as $\lambda_{0uw}/|z|$, in both downwind or crosswind directions (cf. top panels to bottom panels). This suggests that much of the turbulent heat transport in the ocean surface boundary layer is accomplished by the same eddies that transport momentum, which is consistent with the turbulent Prandtl number being approximately 1. Fourth, in the downwind measurements both λ_{0uw} and λ_{0Tw} decrease slightly for $|z|/L > 0$, consistent with the notion that stratification reduces the turbulent length scale.

e. Comparison of length scale measurements

The turbulent length scales presented above were estimated from cospectra using the frozen turbulence hypothesis, and they can be compared with measurements made using the spatial array of sensors. We make this comparison by examining the decay of the cross-covariance function across the ADV array. The array had four ADVs at 2.2-m depth, from which six unique sensor spacings can be made. This enables us to estimate $E(r)$, the even part of the cross-covariance func-

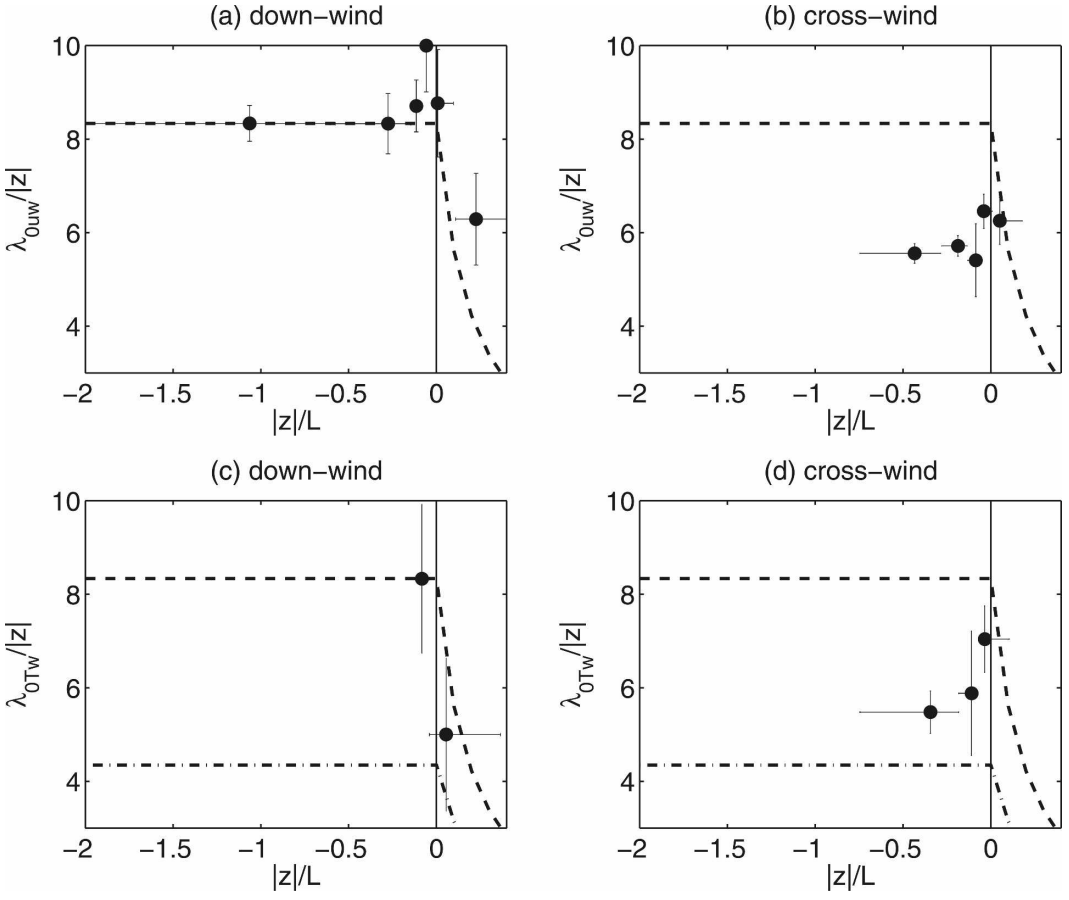

FIG. 9. Here, $\lambda_0/|z|$ vs $|z|/L$. Dots are bin medians of observations, formed from a constant number of observations per bin; the dashed lines are the momentum results of Wyngaard and Coté (1972) [(15) in this study]; and (c),(d) the dash–dot lines are the temperature results of Wyngaard and Coté (1972) [(16) in this study]. Vertical error bars show two standard errors of the distribution of observations within each bin, and horizontal bars show the range of $|z|/L$ in each bin. (a),(c) The $\lambda_0/|z|$ when the wind was aligned with the drift and (b),(d) $\lambda_0/|z|$ when the wind was across the drift; (a),(b) $\lambda_{0uw}/|z|$ and (c),(d) $\lambda_{0Tw}/|z|$. At a nominal depth of 2.2 m, the dominant length scales shown in this figure range between ~10 and 20 m. This size range is consistent with the horizontal scales of Langmuir circulation during CBLAST determined by inspection of surface convergence velocities obtained from a fanbeam ADCP (cf. Plueddemann et al. 2001).

tion of u' and w', at six values of sensor separation r. Here $E(r)$ is defined as

$$E(r) = \frac{1}{2}[\overline{u'(\mathbf{x})w'(\mathbf{x}+\mathbf{r})} + \overline{u'(\mathbf{x}+\mathbf{r})w'(\mathbf{x})}]. \quad (17)$$

Position is $\mathbf{x}$, the vector separation between sensors is $\mathbf{r}$, and $r = |\mathbf{r}|$. By definition, $E(0) = \overline{u'w'}$.

A prediction of the even part of the cross-covariance function comes from the Fourier transform of model cospectrum [(4)] (Trowbridge and Elgar 2003):

$$\frac{E(r)}{\overline{u'w'}} = \frac{A}{2}\int_{-\infty}^{+\infty} d\xi \frac{\cos\left(\frac{2\pi\xi r}{\lambda_0}\right)}{1+|\xi|^{7/3}}, \quad (18)$$

where ξ is a dummy variable of integration and A is the same as in (4). This integral was evaluated numerically using values of λ_0 determined by the cospectral fitting procedure.

Cross-covariance estimates from the spatial array are contaminated by surface waves in the manner discussed in sections 2c and 2d, so analogous to (8) we computed $E(r)$ by integrating only the below–wave band parts of the spatially lagged cospectra:

$$\overline{u'(\mathbf{x})w'(\mathbf{x}+\mathbf{r})} = \int_0^{k_c} dk \mathrm{Co}_{u(\mathbf{x})w(\mathbf{x}+\mathbf{r})}(k), \quad (19)$$

where u and w were each measured at different ADVs. This allows examination of the spatial coherence of motions with wavenumbers smaller than the wave band

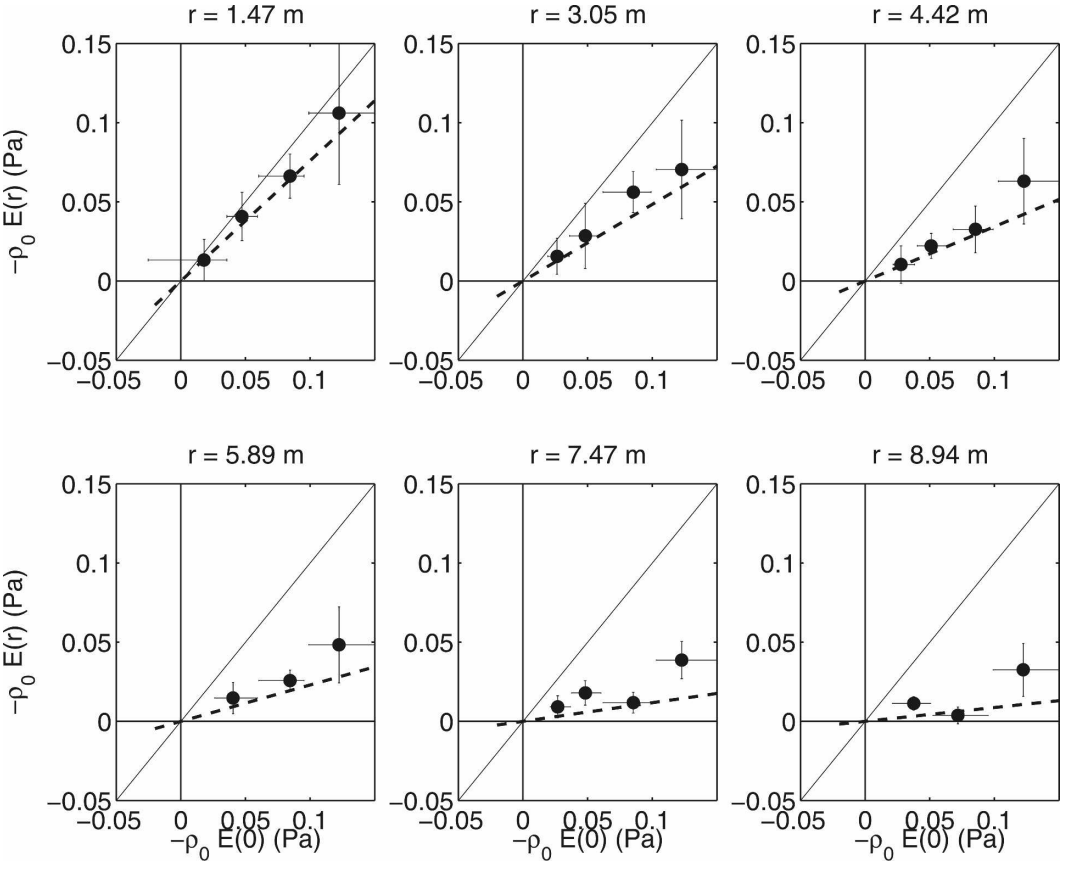

FIG. 10. Plots of $-\rho_0 E(r)$ vs $-\rho_0 E(0)$ in the downwind direction for the six ADV separations in this study. The results shown here are limited to depths of $-2.9\ \text{m} < z < -2.3\ \text{m}$. Dots are bin medians of observations, formed from a constant number of observations per bin. Vertical error bars show two standard errors of the distribution of observations within each bin, and horizontal bars show the range of $E(0)$ in each bin. The black line is 1:1. The dashed line is the expected relationship from (18). The rolloff wavenumber used for these expected relationships is the median value of the observed downwind λ_0.

cutoff k_c (Fig. 4). Using only the below–wave band part of the spectrum should not inhibit this analysis because, as discussed in section 2d, these scales capture most of the energy of the cospectra. In addition, we are examining not the magnitude of $E(r)$, but the ratio $E(r)/E(0)$, and the model prediction of that ratio does not change significantly if we use only the below–wave band portion of the spectrum rather than the complete spectrum.

Like the length scales estimated from cospectra, the observations from the spatial array show that the turbulence is coherent over much larger distances in the downwind direction than in the crosswind direction. Measurements of $E(r)$ versus $E(0)$ from the spatial array show that in the downwind direction the turbulence decays over spatial scales similar to, but slightly larger than, those predicted by (18) using the length scales from the cospectral estimates (Fig. 10). In the crosswind direction, $E(r)/E(0)$ decays more quickly in measurements from the spatial array than is predicted from (18) (Fig. 11). The predictions of $E(r)/E(0)$, shown as dashed lines, were based on the median λ_0 for a depth bin between 2.3 and 2.9 m during unstable conditions ($|z|/L < 0$), when $\lambda_0/|z|$ is roughly constant. Using a least squares fit of the observed $E(r)/E(0)$ to the model covariance function (18), we were able to determine average values for $\lambda_0/|z|$ from the measurement array during unstable periods. In the downwind direction, the estimate from the spatial array is $\lambda_0/|z| = 11.5$, similar to, but slightly larger than, the Wyngaard and Coté prediction [Fig. 9 and (15)]. In the crosswind direction (using only the three shortest sensor separations in the average), $\lambda_0/|z| = 5$.

4. Discussion

We have estimated turbulent fluxes of momentum and heat, as well as the length scales of the dominant flux-carrying eddies. The downwind length scales are in agreement with atmospheric observations (Wyngaard

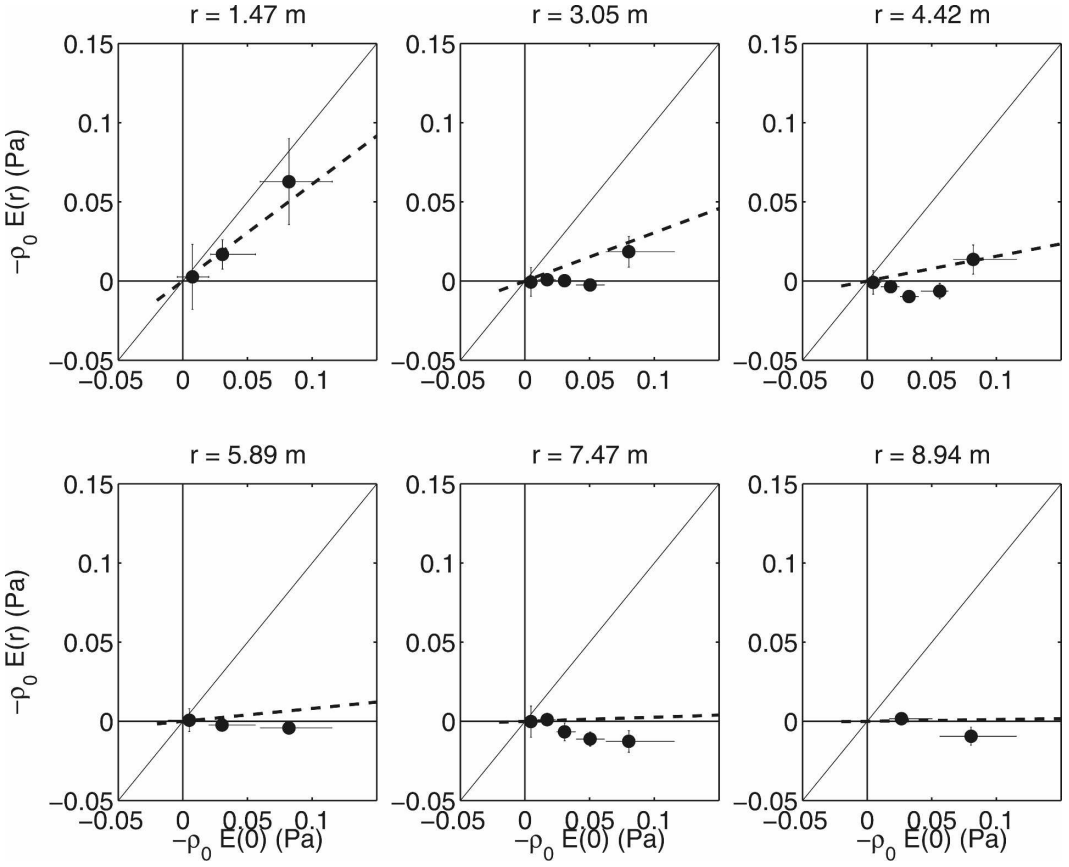

FIG. 11. Plots of $-\rho_0 E(r)$ vs $-\rho_0 E(0)$ in the crosswind for the six ADV separations in this study. These points are limited to depths of -2.9 m $< z < -2.3$ m. Symbols are the same as in Fig. 10, and the dashed lines were made using the median value of the observed crosswind λ_0.

and Coté 1972), and the difference between downwind and crosswind scales is consistent with classical laboratory measurements of turbulence driven by boundary stress (Grant 1958). Taken alone, these measurements do not address the question of whether mixed layer turbulence is affected by the presence of surface waves through Langmuir circulation and wave breaking. However, measurements of the fluxes and mean temperature gradients can be used to test a simple turbulence closure model that does not include these surface wave effects. A more detailed analysis of the range of existing closure models is beyond the scope of this paper and is reserved for future research.

We test the ability of the MO closure model to predict the mean temperature gradient, and we use the same set of equations to estimate the stability function for heat ϕ_h. We compare our estimate to the ϕ_h given by Large et al. [(1994), their Eq. (B1)]. This comparison is made for boundary layer thicknesses greater than 6 m.

As in other turbulence closer models, MO theory predicts

$$\frac{\partial T}{\partial z} = -\frac{\overline{T'w'}}{K_h}; \tag{20}$$

K_h is a turbulent diffusivity that in MO theory is defined as

$$K_h = \frac{u_* \kappa |z|}{\phi_h}, \tag{21}$$

where $u_* = \sqrt{\tau/\rho_0}$. The null hypothesis in this comparison is that Langmuir circulation and wave breaking have no effect on mixed layer structure, and that the temperature gradient predictions of (20) will agree with the observed gradients. If the surface wave processes do play a role in homogenizing the mixed layer, we expect that the temperature gradients from (20) will be larger than the measured values.

The observations and model were compared by computing a temperature difference ΔT between 1.4 and 3.2 m, which are the depths of the MicroCAT temperature sensors above and below the ADV/thermistor ar-

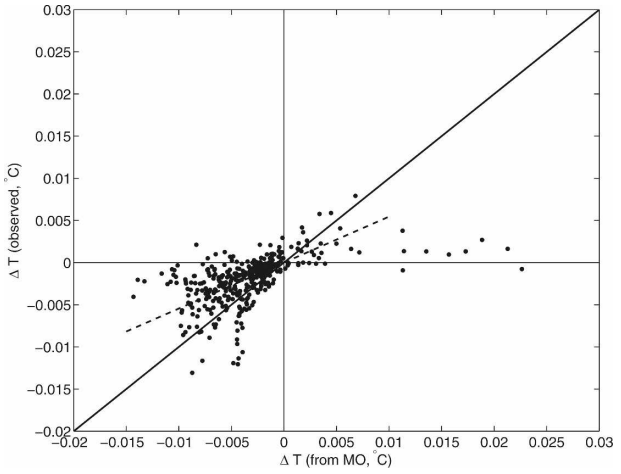

FIG. 12. Observed and predicted temperature difference between MicroCATs at 1.4- and 3.2-m depth. Negative values of ΔT are statically unstable, and positive values are statically stable. Predictions were made using Monin–Obukhov length scales derived from the budget estimates of heat and momentum fluxes. The solid line is 1:1. The dashed line is a best fit to data over the domain shown by the horizontal extent of the line.

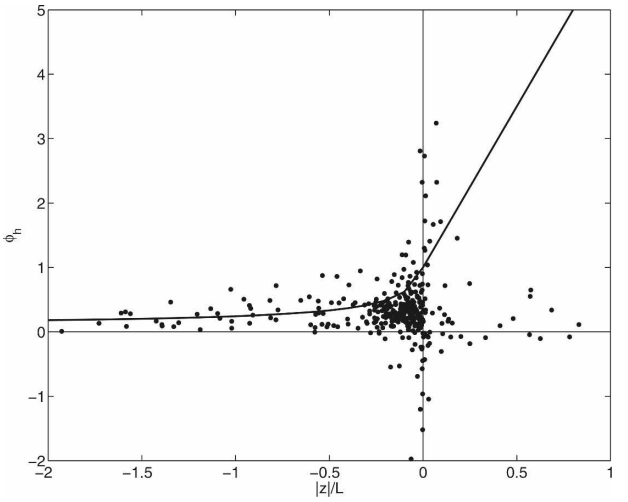

FIG. 13. Comparison of modeled and observed stability functions for heat ϕ_h. The line is from the expression of Large et al. [1994, see their Eq. (B1)] and the dots are observations in the present study.

ray. For the model prediction, the depth z in (20) was taken as 2.3 m. The comparison shows that the temperature gradient in the mixed layer is about half as large as the gradient predicted by MO over most of the range of expected ΔT (Fig. 12). At large predicted ΔT, however, the modest number of observations is more substantially smaller than the MO predictions. These observations show that the ocean mixed layer is much more effectively mixed than is predicted by standard boundary layer theories.

The stability function was estimated as

$$\phi_h = \frac{\Delta T}{\Delta z} \frac{u_* \kappa |z|}{T'w'}, \tag{22}$$

using the same sensor separation as above. In stable, near-neutral, and weakly unstable conditions ($-0.3 < |z|/L$) the estimates of ϕ_h from our observations are usually smaller than the values given by Large et al. (1994), which is consistent with the observed temperature gradient being smaller than predicted (Fig. 13). In more strongly unstable conditions ($|z|/L < -0.3$) the observed ϕ_h are similar to those given by Large et al. (1994).

The enhanced mixing in the mixed layer is likely a consequence of turbulence generation by wave breaking and Langmuir circulation, which are included neither in MO nor in classic forms of most closure models. The enhanced mixing is consistent with expectations from previous studies of those processes. Langmuir circulation has been predicted by LES models to produce much gentler temperature gradients than rigid-boundary processes alone (McWilliams et al. 1997; Li et al. 2005), and our observations were also made in a depth range predicted by Terray et al. (1996) to have enhanced turbulent dissipation rates associated with wave breaking. Either, or both, of these processes could be responsible for the small observed temperature gradients.

5. Conclusions

Cospectra of uw and Tw were measured for fluctuations in the ocean surface boundary layer. A two-parameter model cospectrum developed for the bottom boundary layer of the atmosphere fits the below–wave band portion of the observed spectra, suggesting similar spectral shapes for both atmospheric boundary layer and ocean surface boundary layer turbulence.

By fitting this model cospectrum to observed cospectra, a new method was developed to estimate turbulent fluxes of heat and momentum. These cospectral turbulent fluxes were used to close momentum and heat budgets across the air–sea interface. To our knowledge, these are the first direct measurements of turbulent fluxes in the mixed layer to do this successfully.

Length scales of the dominant flux-carrying eddies were also estimated from the fits of the model spectrum. Consistent with laboratory and atmospheric measurements, the downwind length scales were larger than the crosswind length scales, and the downwind scales were smaller under stabilizing buoyancy forcing than

under unstable buoyancy forcing. The cospectral estimates of length scale were consistent with estimates made by examining the decay of the cross-covariance function along the array of ADVs.

The flux estimates were used to compare measured temperature gradients with temperature gradients computed using Monin–Obukhov similarity theory, and to compare observations of ϕ_h with those suggested by Large et al. (1994). The observed temperature gradients and stability functions were smaller than the predictions. This homogenization of the mixed layer is likely to be caused by the presence of turbulence generated by mechanisms not accounted for in MO theory: Langmuir circulation and wave breaking.

Acknowledgments. We thank Albert J. Williams III, Ed Hobart, and Neil McPhee for assistance in development and deployment of the instruments, and we are grateful to the Office of Naval Research for funding this work as a part of CBLAST-Low. We also appreciate the comments of two anonymous reviewers who provided helpful comments that improved the quality of the manuscript.

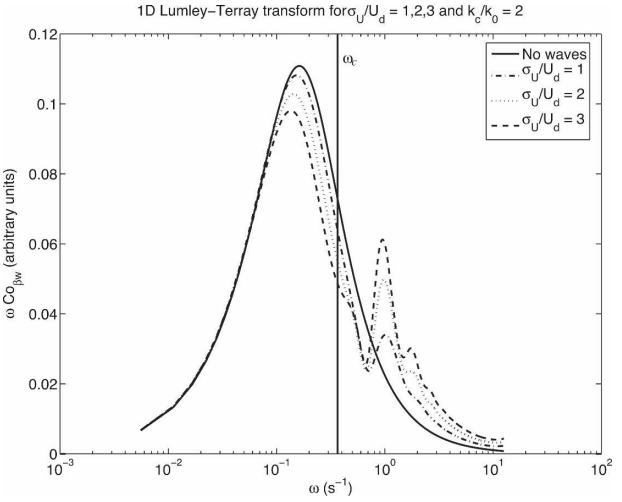

FIG. A1. Frequency domain variance-preserving cospectra of unsteadily advected frozen turbulence whose wavenumber spectrum is described by (4). The wave band cutoff, ω_c, is shown by the vertical line at $\approx 0.38\ \mathrm{s}^{-1}$. As the wave energy increases, the effects of the unsteady advection shift more energy from below–wave band frequencies to wave band frequencies and decrease the apparent rolloff frequency.

APPENDIX

Effects of Unsteady Advection

In the steadily advected frozen turbulence hypothesis (Taylor 1938), the frequency response to turbulent motions at a fixed location is determined by the size of the turbulent eddies and the rate at which they move past the sensor. In the presence of surface waves, however, turbulent eddies move in much more complicated patterns as they are carried by the wave orbits, and the simple relationship (5) no longer holds. Lumley and Terray (1983) discussed the consequences of this unsteady advection for the case of isotropic turbulence, and Trowbridge and Elgar (2001) extended and compared their predictions to observations in the bottom boundary layer. The qualitative effect of the unsteady advection on frequency spectra is to shift energy from where it would have been expected in steadily advected spectra. In particular, some energy that would have appeared at frequencies *lower than* the wave band, if advection were steady, is found *in* the wave band in the case of unsteady advection.

We have developed a model to test the effects of unsteady advection on the frequency domain representation of turbulence whose spatial structure is described by (4). In this simplified model, wave and drift motion are restricted to a single horizontal direction, x. This restricted form of wave advection was chosen largely because of the lack of a model of the three-dimension spatial structure of the turbulence. It is expected that the qualitative effects of fully three-dimensional motions will be similar.

Combining Eqs. (2.2), (2.6), and (2.17) of Lumley and Terray (1983) and (4) one can predict the frequency domain cospectrum, $\mathrm{Ko}_{\beta w}(\omega)$, expected in the presence of this 1D unsteady advection:

$$\mathrm{Ko}_{\beta w}(\omega) = \frac{1}{2\pi}\int_{-\infty}^{+\infty} d\mathcal{T}\int_{-\infty}^{+\infty} dk\,\frac{\mathrm{Co}_{\beta w}(k)}{2} \times e^{i\mathcal{T}(kU_d-\omega)}e^{k^2[c(\mathcal{T})-c(0)]}. \tag{A1}$$

The temporal autocorrelation function of the wave displacements, $c(\mathcal{T})$, can be estimated from observed horizontal velocity spectra as

$$c(\mathcal{T}) = \frac{1}{2\pi}\int_{-\omega_{\max}}^{+\omega_{\max}} d\omega\, e^{i\omega\mathcal{T}}\frac{S_{uu}(\omega)+S_{vv}(\omega)}{\omega^2}, \tag{A2}$$

where S_{uu} and S_{vv} are two-sided autospectra of the horizontal velocities. To examine the effects of increasingly large waves, we computed the transformation for several values of σ_U/U_d, where σ_U is the standard deviation of wave velocities and U_d is the steady drift speed.

Compared with the frequency cospectrum in the case of steadily advected frozen turbulence, the frequency

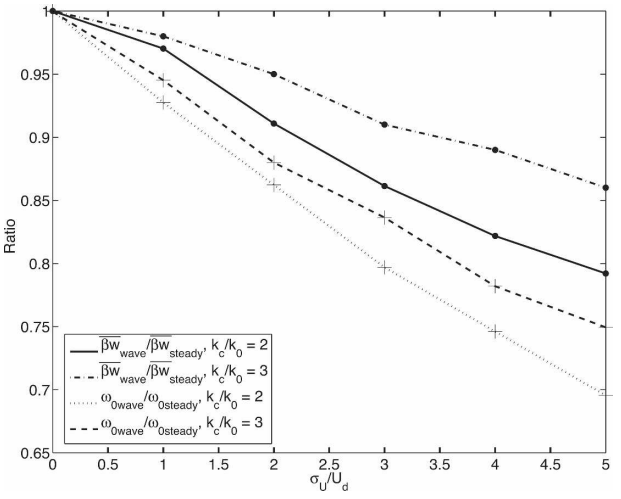

FIG. A2. Ratios of covariance and rolloff frequency estimated under unsteady advection to those expected under steady advection. Relative to the estimates under steady advection, the quality of the estimates of $\overline{\beta' w'}$ and ω_0 under unsteady advection decreases in the presence of increased relative wave energy (larger σ_U/U_d) and higher relative rolloff wavenumber (smaller k_c/k_0).

cospectrum of unsteadily advected frozen turbulence has somewhat less energy below the wave band and correspondingly more energy in the wave band (Fig. A1). The magnitude of the distortion is a function of σ_U/U_d, and the proximity of the cutoff wavenumber to the rolloff wavenumber, k_c/k_0. The location of the peak of the variance-preserving spectrum, approximately ω_0, is decreased by this change in energy distribution. At larger relative wave energies (larger σ_U/U_d), and in spectra when the rolloff is closer to the cutoff (smaller k_c/k_0), errors in estimating the covariance and the rolloff frequency are larger (Fig. A2). To investigate the magnitude of the estimation error we fit the spectra described by (A1) (Fig. A1) in the same way as described in section 2d. Figure A2 compares the resulting estimates of covariance and ω_0 to the values expected in the case of steady advection.

For $\sigma_U/U_d \leq 2$ and $k_c/k_0 > 2$, this 1D model suggests that the estimates of rolloff frequency and covariance should be within 15% of the values expected by assuming frozen turbulence advected with a constant velocity, U_d. We therefore limit our observations to times when $\sigma_U/U_d \leq 2$ and use the steadily advected form of frozen turbulence (5) to transform our frequency observations into wavenumber observations.

REFERENCES

Agrawal, Y. C., E. A. Terray, M. A. Donelan, P. A. Hwang, A. J. Williams III, W. M. Drennan, K. K. Kahma, and S. A. Kitaigorodskii, 1992: Enhanced dissipation of kinetic energy beneath surface waves. *Nature,* **359,** 219–220.

Bendat, J. S., and A. G. Piersol, 2000: *Random Data: Analysis and Measurement Procedures.* 3rd ed. John Wiley and Sons, 594 pp.

Cavaleri, L., and S. Zecchetto, 1987: Reynolds stress under wind waves. *J. Geophys. Res.,* **92** (C4), 3894–3904.

Craig, P. D., and M. L. Banner, 1994: Modeling wave enhanced turbulence in the ocean surface layer. *J. Phys. Oceanogr.,* **24,** 2546–2559.

Edson, J. B., and Coauthors, 2007: The coupled boundary layers and air-sea transfer experiment in low winds. *Bull. Amer. Meteor. Soc.,* **88,** 341–356.

Ekman, V. W., 1905: On the influence of the earth's rotation on ocean currents. *Arkiv Mat. Astron. Fys.,* **2** (11), 1–53.

Fairall, C., E. Bradley, J. Hare, A. Grachev, and J. Edson, 2003: Bulk parameterizations of air–sea fluxes: Updates and verification for the COARE algorithm. *J. Climate,* **16,** 571–591.

Grant, H. L., 1958: The large eddies of turbulent motion. *J. Fluid Mech.,* **4,** 149–190.

Hanjalic, K., and B. E. Launder, 1972: A reynolds stress model of turbulence and its application to thin shear flows. *J. Fluid Mech.,* **52,** 609–638.

Hasselmann, K., 1970: Wave-driven intertial oscillations. *Geophys. Fluid Dyn.,* **1,** 463–502.

Jerlov, N., 1968: *Optical Oceanography.* Elsevier, 194 pp.

Jones, W. P., and B. E. Launder, 1972: The prediction of laminerization with a two-equation model of turbulence. *Int. J. Heat Mass Transfer,* **15,** 301–314.

Kaimal, J., J. C. Wyngaard, Y. Izumi, and O. R. Cote, 1972: Spectral characteristics of surface-layer turbulence. *Quart. J. Roy. Meteor. Soc.,* **98,** 563–589.

Kantha, L. H., and C. A. Clayson, 2004: On the effect of surface gravity waves on mixing in the oceanic mixed layer. *Ocean Modell.,* **6,** 101–124.

Kristensen, L., J. Mann, S. Oncley, and J. Wyngaard, 1997: How close is close enough when measuring scalar fluxes with displaced sensors? *J. Atmos. Oceanic Technol.,* **14,** 814–821.

Large, W. G., J. C. McWilliams, and S. C. Doney, 1994: Oceanic vertical mixing: A review and a model with a nonlocal boundary layer parameterization. *Rev. Geophys.,* **32,** 363–403.

Lentz, S. J., 1992: The surface boundary layer in coastal upwelling regions. *J. Phys. Oceanogr.,* **22,** 1517–1539.

——, 1995: Sensitivity of the inner-shelf circulation to the form of the eddy viscosity profile. *J. Phys. Oceanogr.,* **25,** 19–28.

Li, M., C. Garrett, and E. Skyllingstad, 2005: A regime diagram for classifying turbulent large eddies in the upper ocean. *Deep-Sea Res. I,* **52,** 259–278.

Lumley, J., and E. Terray, 1983: Kinematics of turbulence convected by a random wave field. *J. Phys. Oceanogr.,* **13,** 2000–2007.

Madsen, O. S., 1977: A realistic model of the wind-induced Ekman boundary layer. *J. Phys. Oceanogr.,* **7,** 248–255.

McWilliams, J. C., and J. M. Restrepo, 1999: The wave-driven ocean circulation. *J. Phys. Oceanogr.,* **29,** 2523–2540.

——, P. P. Sullivan, and C.-H. Moeng, 1997: Langmuir turbulence in the ocean. *J. Fluid Mech.,* **334,** 1–30.

Mei, C. C., 1989: *The Applied Dynamics of Ocean Surface Waves.* World Scientific, 760 pp.

Mellor, G. L., 2003: The three-dimensional current and surface wave equations. *J. Phys. Oceanogr.,* **33,** 1978–1989.

——, and T. Yamada, 1982: Development of a turbulence closure

model for geophysical fluid problems. *Rev. Geophys.,* **20,** 851–875.

Melville, W. K., F. Veron, and C. J. White, 2002: The velocity field under breaking waves: Coherent structures and turbulence. *J. Fluid Mech.,* **454,** 203–233.

Monin, A. S., and A. M. Yaglom, 1971: *Statistical Fluid Mechanics: Mechanics of Turbulence.* The MIT Press, 1643 pp.

Paulson, C., and J. Simpson, 1977: Irradiance measurements in the upper ocean. *J. Phys. Oceanogr.,* **7,** 952–956.

Plueddemann, A. J., and R. A. Weller, 1999: Structure and evolution of the oceanic surface boundary layer during the Surface Waves Processes Program. *J. Mar. Syst.,* **21,** 85–102.

——, E. A. Terray, and R. Merrewether, 2001: Design and performance of a self-contained fan-beam ADCP. *IEEE J. Oceanic Eng.,* **26,** 252–258.

Polton, J., D. Lewis, and S. Belcher, 2005: The role of wave-induced Coriolis–Stokes forcing on the wind-driven mixed layer. *J. Phys. Oceanogr.,* **35,** 444–457.

Santala, M. J., 1991: *Surface-Referenced Current Meter Measurements*. Ph.D. thesis, Massachusetts Institute of Technology/Woods Hole Oceanographic Institution, 280 pp.

Shaw, W. J., and J. H. Trowbridge, 2001: The direct estimation of near-bottom turbulent fluxes in the presence of energetic wave motions. *J. Atmos. Oceanic Technol.,* **18,** 1540–1557.

——, ——, and A. J. Williams III, 2001: Budgets of turbulent kinetic energy and scalar variance in the continental shelf bottom boundary layer. *J. Geophys. Res.,* **18** (C5), 9551–9564.

Soulsby, R., 1980: Selecting record length and digitization rate for near-bed turbulence measurements. *J. Phys. Oceanogr.,* **10,** 208–219.

Taylor, G. I., 1938: The spectrum of turbulence. *Proc. Roy. Soc. London,* **A164,** 476–490.

Terray, E. A., M. A. Donelan, Y. C. Agrawal, W. M. Drennan, K. K. Kahma, A. J. Williams III, P. A. Hwang, and S. A. Kitaigorodskii, 1996: Estimates of kinetic energy dissipation under breaking waves. *J. Phys. Oceanogr.,* **26,** 792–807.

——, W. M. Drennan, and M. A. Donelan, 1999: The vertical structure of shear and dissipation in the ocean surface layer. *Proc. Symp. on the Wind-Driven Air-Sea Interface—Electromagnetic and Acoustic Sensing, Wave Dynamics, and Turbulent Fluxes,* Sydney, Australia, University of New South Wales, 239–245.

Thais, L., and J. Magnaudet, 1996: Turbulent structure beneath surface gravity waves sheared by the wind. *J. Fluid Mech.,* **328,** 313–344.

Trowbridge, J. H., 1998: On a technique for measurement of turbulent shear stress in the presence of surface waves. *J. Atmos. Oceanic Technol.,* **15,** 290–298.

——, and S. Elgar, 2001: Turbulence measurements in the surf zone. *J. Phys. Oceanogr.,* **31,** 2403–2417.

——, and ——, 2003: Spatial scales of stress-carrying nearshore turbulence. *J. Phys. Oceanogr.,* **33,** 1122–1128.

Veron, F., and W. K. Melville, 2001: Experiments on the stability and transition of wind-driven water surfaces. *J. Fluid Mech.,* **446,** 25–65.

Wilcox, D., 1988: Reassessment of the scale-determining equation for advanced turbulence models. *Amer. Inst. Aeronaut. Astron. J.,* **26,** 1299–1310.

Wilczak, J., and J. Tillman, 1980: The three-dimensional structure of convection in the atmospheric surface layer. *J. Atmos. Sci.,* **37,** 2424–2443.

Wyngaard, J., and O. Coté, 1972: Cospectral similarity in the atmospheric surface layer. *Quart. J. Roy. Meteor. Soc.,* **98,** 590–603.